



Full length article

Single image dehazing using a new color channel[☆]Geet Sahu ^a, Ayan Seal ^{a,b,*}, Ondrej Krejcar ^{b,c}, Anis Yazidi ^d^a PDPM Indian Institute of Information Technology, Design and Manufacturing, Jabalpur, 482005, India^b Center for Basic and Applied Science, Faculty of Informatics and Management, University of Hradec Kralove, Rokitanskeho 62, 500 03 Hradec Kralove, Czech Republic^c Malaysia-Japan International Institute of Technology (MJIIT), Universiti Teknologi Malaysia, Jalan Sultan Yahya Petra, 54100 Kuala Lumpur, Malaysia^d Research Group in Applied Artificial Intelligence, Oslo Metropolitan University, 460167, Norway

ARTICLE INFO

Keywords:

Image dehazing
Atmospheric light
Radiance
Illuminance scaling factor

ABSTRACT

Images with hazy scene suffer from low-contrast, which reduces the visible quality of the scene, thus making object detection a more challenging task. Low-contrast can result from foggy weather conditions during image acquisition. Dehazing is a process of removal of haze from the photography of a hazy scene. Single-image dehazing based on dark channel priors are well-known techniques in this field. However, the performance of such techniques is limited to priors or constraints. Moreover, this type of method fails when images have sky-region. So, a method is proposed, which can restore the visibility of hazy images. First, a hazy image is divided into blocks of size 32×32 , then the score of each block is calculated to select a block having the highest score. Atmospheric light is calculated from the selected block. A new color channel is considered to remove atmospheric scattering, obtained channel value and atmospheric light are then used to calculate the transmission map in the second step. Third, radiance is computed using a transmission map and atmospheric light. The illumination scaling factor is adopted to enhance the quality of a dehazed image in the final step. Experiments are performed on six datasets namely, I-HAZE, O-HAZE, BSDS500, FRIDA, RESIDE dataset and natural images from Google. The proposed method is compared against 11 state-of-the-art methods. The performance is analyzed using fourteen quantitative evaluation metrics. All the results demonstrate that the proposed method outperforms 11 state-of-the-art methods in most of the cases.

1. Introduction

Natural images and their perception play an important role in image visualization and understanding. Bright images can improve the precision of computer vision applications such as surveillance [1], object detection [2], image classification [3], image/video retrieval [4], and land cover identification in remote sensing images [5] through proper understanding. Therefore, a clear image is an essential requirement in image processing and computer vision-based tasks. However, it is always hard to capture clear images, especially in degraded visibility conditions. Haze present in the atmosphere degrades the visibility of images drastically. It could be in the form of fog, smoke, dust, or mist. The haze particles pervert or sometimes completely cease the light rays emanating from the image. Light rays scatter in different directions when they strike with atmospheric particles. The amount of scattering depends on the distance between the image and the camera. Although haze is a natural phenomenon, most cameras cannot always cope up with such type of environment. The camera captures the

light coming from the image, blended with light coming from other directions called the airlight. Haze in images results in faded color, low contrast, and loss in the visibility of the image. Reduction of visibility in images causes a problem in camera-guided vehicles, autonomous vehicle and navigation based systems. Depth analysis, color preservation and visibility enhancement are the challenging tasks for dehazing. Therefore, an efficient algorithm is needed to remove haze from the captured scenes and thus for making computer vision applications more reliable.

In [6], Koschmieder presented an image formation model, also known as the degradation model that is widely used in dehazing. Eq. (1) is used to formally describe the model. It consists of two atmospheric scattering characteristics namely, direct attenuation and airlight. The former one describes the amount of unscattered light, $J(m)t(m)$, which travels directly from the image to the camera. In contrast, the latter one, $A(1-t(m))$, is the amount of light coming from the scattered atmospheric particle. The degradation model is also portrayed in Fig. 1, where the

[☆] This paper has been recommended for acceptance by Zicheng Liu.

* Corresponding author at: PDPM Indian Institute of Information Technology, Design and Manufacturing, Jabalpur, 482005, India.

E-mail address: ayan@iiitdmj.ac.in (A. Seal).

blue and red dashed lines denote the direct attenuation and airlight respectively.

$$I(m) = J(m)t(m) + A(1 - t(m)), \quad (1)$$

where I is the captured hazy scene, J is the scene radiance which is needed to recover, t is the medium transmission. The function t in the above equation can be expressed as $t(m) = e^{\beta * d(m)}$, where β is atmospheric scattering coefficient and $d(m)$ is the distance between an object and a camera, A is the global atmospheric light, and m is the pixel coordinates.

Existing image dehazing methods can be broadly classified into groups: traditional approaches and learning-based methods. Traditional methods are further categorized into the method based on a physical models such as polarimetric image dehazing [7–9] and image enhancement method such as linear transformation [10], structure-preserving [11], histogram-based [12,13], wavelet-based [14,15], retinex methods [16–18] and dark channel prior (DCP) [19–24]. Similarly, learning-based methods use machine learning and deep learning approaches [25–31] for dehazing. All the above mentioned methods are discussed here briefly. Polarimetric methods depend on the degree of polarization. Different methods considered this phenomenon for dehazing. Schechner et al. [7] and Shwartz et al. [8] presented polarized filters-based methods. Multiple images of the same scene having different degrees of polarization are required for these methods. However, these methods fail since polarizing filters are not able to gain rapid changes in the scene. These techniques [7,8] used multiple images of the same scene, which is difficult to capture in real-time. Therefore, single image dehazing methods [20,21,25,26] are getting more attention in recent years. However, all these works are based on some assumptions. In [32], Gao et al. presented a multi-focus fusion method for dehazing. First, an atmospheric light was estimated from the sky region, then a fast local Laplacian filtering with adaptive boundary constraint was introduced to refine the transmission map by reducing oversaturation in the image. Finally, a multi-focus image fusion method was applied to recover the image. Qi et al. [11] discussed a structure-preserving method for dehazing. First, the minimum channel of the hazy image was estimated, then the structure detail of the minimum channel was considered as a reference image. The minimum channel was filtered to derive an initial airlight, which was refined further by joint bilateral filter guided by reference image. Atmospheric light was calculated using a quad-tree subdivision method. Finally, radiance was stored using the atmospheric attenuation model. Further, the histogram equalization (HE) method was explored to enhance the contrast of a hazy image by increasing the gray distribution of images. In [12,13], contrast limited adaptive HE was combined with the finite impulse response filter and weiner filter to enhance the contrast of images. However, the performance of HE method is not satisfactory for color images. The wavelet transform method is considered for image dehazing. He et al. [14] offered an optical model and regularized optimization for restoring images. First, they converted non-convex, bilinear problem to a convex, linear optimization problem by estimating the atmosphere light constant and then they applied multilevel Haar wavelet transform. The optimization was achieved by applying the algorithm to the low-frequency sub-band decomposition of the original image to accelerate the processing speed. Further, Khmag et al. [15] employed mean vector L2-norm to estimate the transmission map and enhanced it by second-generation wavelet transform filter. However, color-shift occurred in the resulting images. Moreover, the Retinex based methods were also considered for image enhancement. The principal concept of the Retinex method is to derive reflectance and illuminance component of an image which is further used to remove haze. Yang et al. [16] combined sub-block local information using an adaptive filter to calculate the luminance of an image. Further, Hu et al. [17] utilized bilateral filtering to estimate the illumination component. In [18], Shu et al. presented a multi-scale Retinex image enhancement method on sub-band image decomposition to enhance

the contrast of the image. Retinex methods are easy to implement, however, it causes a halo effect in images and make it too bright. Further, He et al. [19] described a DCP method for single image dehazing. According to the DCP method, most of the local patches in outdoor haze-free color images have very low-intensity values in at least one color channel. Transmission map and atmospheric light were estimated based on the above said assumption. However, the DCP does not work well if the image consists of a sky region [33]. Galdran [34] dehazed the image without estimating the transmission map. The gamma correction operations were employed to artificially under-expose images. Further, the images were dehazed using a multi-scale Laplacian blending scheme. Fang [35] presented a fast variational method. First, the transmission map was estimated by a window based adaptive method based on the celebrated DCP. The transmission map was then converted into a depth map to built a new variational model and restore the image. Later, Wang et al. [36] combined the DCP with the total variation models namely, layered total variation, multichannel total variation, and color total variation regularizers, for dehazing. Fast split Bregman algorithms were explained to improve the efficiency of the models. Further, Hou et al. [37,38] considered the DCP method in underwater images by employing underwater total variation models to restore images. Recently, learning-based methods are gaining attention due to their ability to learn features automatically. Tang et al. [25] used the random forest to estimate the transmission map and refined it by a guided filter. Further, the image degradation model and white balance restoration were exploited to restore the image. In [26], Zhu et al. presented a color attenuation prior and linear model to estimate the depth map. They utilized supervised learning to learn model parameters, which helped to better estimate the transmission map. In [27], Gui et al. exploited Support Vector Machine (SVM) for dehazing. First, the feature vectors were extracted using the dark channel histogram and texture features of the hazy images. The feature vectors were then trained by the SVM algorithm to realize the automatic binary classification of images. Second, the dehazing methods processed the classified hazy image and the dehazed image was evaluated based on the performance of different dehazing methods. Finally, this model helped to produce a better dehazed image. Further, in [28], Cai et al. presented DehazeNet to extract features from hazy images and used non-linear functions to estimate the transmission map of the input image. Moreover, Ren et al. [29] suggested a multi-scale convolutional neural network, which computes a coarse transmission map using coarseNet, then feeds the resultant transmission map to the second CNN of FineNet to refine transmission map. Since the above mentioned models uses CNN to estimate the transmission map and further process it to get a dehazed image, therefore, Li et al. [30] and Guo et al. [31] presented dehazing network to predict a dehazed image directly. Although deep learning-based methods give better results. However, these methods suffer from several problems [39]. First, they require immense amount of training time. Second, they are greedy in terms of data, meaning they require a huge amount of data. Finally, most of the models are trained on synthetic data. Hence, the generalization problem can occur.

Therefore, a new DCP based method is introduced for dehazing images in this study. The salient contributions are as follows:

- Atmospheric light is estimated by dividing an image into blocks, then the score of each block is computed. The block having the highest score is further picked for calculating the atmospheric light.
- A new color model is adopted to calculate the transmission map, which is further used for computing radiance.
- At last, we enhance the dehazed image using the illuminance scaling factor to improve its visibility.

Since the complexity of deep learning-based methods are relatively high in terms of time and data, only traditional methods are considered for comparison in this study. All the experiments are performed on

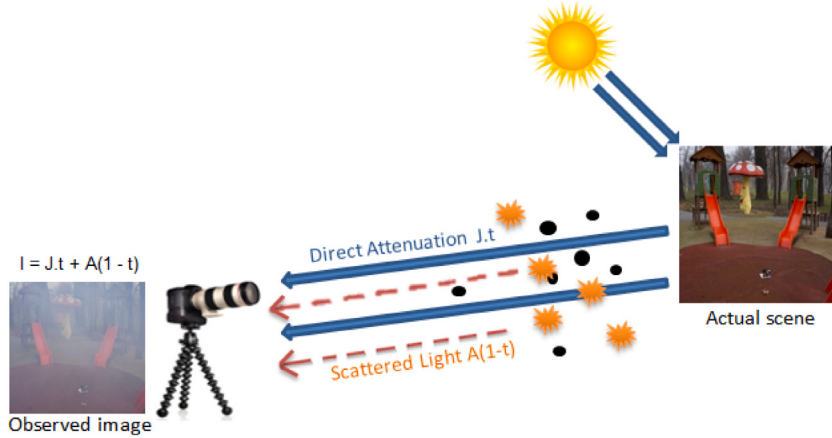


Fig. 1. Image degradation model. (For interpretation of the references to color in this figure legend, the reader is referred to the web version of this article.)

six publicly available benchmark datasets namely, O-HAZE [40], I-HAZE [41], Berkeley Segmentation Dataset (BSDS500) [42], REalistic Single Image DEhazing (RESIDE) [43], Foggy Road Image DAtabase (FRIDA) [44] and natural hazy images from Google. The proposed method is compared with 11 state-of-the-art methods based on ten full reference and six no-reference quality assessment metrics. The empirical results illustrate that the proposed DCP based method outperforms 11 state-of-the-art methods in most of the cases.

The rest of the work is organized as follows: Section 2 describes the material and methods used in this work. A new color model to estimate the transmission map and a novel method to calculate atmospheric light are described in Section 3. Experimental results are reported in Section 4. The proposed method is also compared with eleven state-of-the-art methods in Section 4. Finally, Section 5 concludes this work.

2. Material and method

This section first discusses the DCP method followed by a detailed survey of the DCP based state-of-the-art methods.

2.1. DCP method

Based on the fact that haze depends on unknown depth, dehazing is therefore very challenging. Many methods were presented to measure the depth of haze. One of the popular methods is DCP. This method is based on the statistics of haze-free outdoor images. It is observed that most of the RGB images have very low-intensity pixels in at least one color channel of the non-sky patches. The thickness of the haze can be estimated directly using prior information, which helps further to generate a haze-free image. Algorithm 1 describes the approach used by He et al. [19] to obtain a dehazed image. All the steps of DCP method are as follows:

• Dark Channel

He et al. [19] experimented to investigate the features of haze-free images. They observed that there are some pixels whose intensity values are nearly zero in a local patch of the image. Moreover, they formed a separate channel comprising of these low-intensity pixels and named it a dark channel that is defined in Eq. (2).

$$J^{dark}(m) = \min_{c \in \{R,G,B\}} (\min_p (J^c(p))), \quad (2)$$

where J is the input image, c is a particular color channel of J , p is a local patch centered at m , J^{dark} is the dark channel of image J and m is the pixel coordinate.

• Atmospheric Light

Atmospheric light was calculated by selecting the top 0.1% brightest pixels from J^{dark} then mapping these chosen values to the input image and the highest intensity pixel was then selected as atmospheric light.

• Transmission map

The transmission map of the image was derived using the degradation model described in Eq. (1). Applying minimum operation patch-wise on both sides of Eq. (1), He et al. got

$$\min_p (I^c(m)) = t(m) \min_p (J^c(m)) + A^c (1 - t(m)), \quad (3)$$

Now, by applying minimum operation channel-wise on Eq. (3), He et al. show

$$\min_c \left(\min_p \left(\frac{I^c(m)}{A^c} \right) \right) = t(m) \min_c \left(\min_p \left(\frac{J^c(m)}{A^c} \right) \right) + (1 - t(m)), \quad (4)$$

Since J^{dark} of the haze-free image tends to zero and atmospheric light is always positive, therefore

$$\min_c \left(\min_p \left(\frac{J^c(m)}{A^c} \right) \right) = 0, \quad (5)$$

Substituting Eq. (5) in Eq. (4), transmission map can be derived as:

$$t(m) = 1 - \min_c \left(\min_p \left(\frac{I^c(m)}{A^c} \right) \right), \quad (6)$$

Since a small amount of haze is always present in natural images, to preserve the naturalness of images, a small amount of haze was introduced in the form of constant ω ($0 < \omega \leq 1$) in Eq. (6):

$$t(m) = 1 - \omega \min_c \left(\min_p \left(\frac{I^c(m)}{A^c} \right) \right), \quad (7)$$

The transmission map was estimated using Eq. (7) contains block effects. Therefore, it was further refined using soft matting to get smooth transmission.

• Radiance

Radiance was calculated using an estimated transmission map and atmospheric light. Radiance is derived from Eq. (1) and can be calculated as shown in Eq. (8).

$$J(m) = \frac{I^c(m) - A^c}{\max(t(m), t_0)} + A^c, \quad (8)$$

The transmission was restricted to a lower bound t_0 , used to preserve a small amount of haze in the restored image.

Algorithm 1 DCP based dehazing method

Input: Hazy Image, I
Output: Radiance, J

- 1: Find dark channel prior of hazy image I , $J^{\text{dark}}(m) = \min_{c \in \{R, G, B\}}(\min_p(J^c(p)))$
- 2: Select 0.1% brightest pixel from J^{dark} .
- 3: Pick highest intensity value from I as atmospheric light.
- 4: Calculate transmission, $t(m) = 1 - \omega \min_c(\min_p(\frac{J^c(m)}{A^c}))$
- 5: Refine transmission using soft matting.
- 6: Finally compute radiance, $J(m) = \frac{J^c(m) - A^c}{\max(t(m), t_0)} + A^c$

Dehazing based on DCP method [19] is useful however, the images obtained after dehazing generally introduce artifacts, halo effects and distortion of edges and color in images. Even the time complexity of this method is very high due to soft matting operation. Estimation of atmospheric light also fails when the image contains some brighter objects and the major drawback of this method is that it is not applicable for images containing sky region. It results in a color-shift in the sky region, which makes images look darker.

2.2. DCP based methods

In literature, there are many methods based on DCP. In this section, we present a few of them briefly. He et al. [19] used DCP and refined transmission map using soft matting, however, their method generates images with artifacts and color distortion. Later, Colores et al. [24] removed artifact using pixel-wise maximum operation in the modified dark channel. Moreover, Zhao et al. [45] presented a Transmission MisEstimated (TME) recognition method to distinguish the TME and non-TME regions. They calculated pixel-wise and patch-wise transmission maps separately, then they combined both transmission maps optimally using a multi-scale optimal fusion scheme to avoid the misestimated transmission region. The multi-scale optimal fusion was used further into patch-wise dehazing to suppress halo artifacts. Tan et al. [46] calculated a coarse transmission map, then refined it using a fine transmission map to remove halo effects. Cheng et al. [47] estimated dark channels using two different patch sizes, one large and another small. The hybrid DCP technique was considered to avoid the generation of artifacts. Xiao and Gan [48] estimated atmospheric light through median filter then refined it using guided joint bilateral filtering to generate a new atmosphere light. This modified atmospheric light removes color distortion from the image. Long et al. [49] exploited a low-pass Gaussian filter to refine atmosphere veil. Lin and Wang [50] considered improved guided filtering to estimate the transmission map. Ancuti and Ancuti [51] applied local white balance and contrast enhancement procedure to remove haze from images. The result yields visually pleasing images however, it is not physically valid. Moreover, Zhu et al. [33] presented a fusion of luminance and DCP method. The luminance of the image was employed to calculate the transmission map of the sky region. They combined the transmission map calculated from the sky and non-sky regions to compute the overall transmission map. Further, they used the DCP method to remove haze from image. However, the method introduced more brightness in the images that are already brighter therefore the dehazed image looks unnatural. Further, Sahu and Seal [52] presented two luminance stretching models to adjust the brightness of the dehazed image to some extent.

After investigating all the existing methods based on DCP, it is observed that the main challenges of dehazing are to estimate the atmospheric light and the transmission map. It is noted that the atmospheric light cannot be precisely determined by just picking x% brightest pixel from the dark channel of the whole image. A previous study [53] revealed that global atmospheric light influences error in calculation. Even the transmission map cannot be generated accurately by only applying dark channel operation on the image. The limitations of the above mentioned DCP based state-of-the-art methods illustrate that there is a chance to devise a DCP based method, which can further enhance the quality of a dehazed image.

3. Proposed work

In this section, the proposed method is discussed for generating a dehazed image from the input hazy image. Several steps associated with the proposed method are shown in Fig. 2. The different steps involved in the proposed method are as follows:

3.1. Atmospheric light

It is clear from Section 2 that the DCP method considered a global approach while estimating an atmospheric light. It is also observed that the global approach suffers from limitations as discussed in the same section. Therefore, instead of considering a global atmospheric light, the proposed method estimates atmospheric light from the local region. Initially, an image, I , is divided into equal-sized blocks, as shown in Fig. 3. Although, it is a challenging task to decide the size of an ideal block, the best block size is determined by conducting several experiments using varying block sizes, b . It is observed that the proposed method achieved the best dehazed images when the block size is 32×32 , which is considered throughout this study. However, the results of all the experiments are beyond the scope of this study. A typical block, B_i , consists of $32 \times 32 = 1024$ pixels. Then the score of each B_i is computed as the average pixel value subtracted by the standard deviation of the pixel values within that block. The candidate block, B_u , marked by green color in Fig. 3, is selected, which has the highest score, Max . Then to avoid the effects of suspended particles, we pick the top 1% of 1024 pixels i.e., 10 brightest pixels of the dark channel of the candidate block. Here, we consider the top 1% brightest pixels instead of 0.1% brightest pixels, since 0.1% will correspond to a single pixel and single pixel can be a noisy pixel which will lead to the wrong estimation of atmospheric light. Further, the selected pixels are mapped to the original image. Then the median value of the selected pixels is computed. We consider the median value as it is less affected by noises or outliers. Finally, the median value is considered as the atmospheric light, A . Algorithm 2 gives a brief description of each step followed to estimate A .

Algorithm 2 Procedure for estimating the atmospheric light

Input: Hazy Image, I
Output: Atmospheric light, A

- 1: Divide the input into blocks of size b . $\triangleright b$ is taken as 32×32
- 2: $Max = 0$
- 3: **for** all blocks, B_i , in I **do**
- 4: $s(i) = \mu(B_i) - \sigma(B_i)$ $\triangleright \mu$ is mean and σ is standard deviation
- 5: $Max = \max(Max, s(i))$
- 6: **end for**
- 7: Select block B_u having Max value
- 8: **for** l=1 to row **do** \triangleright row and col of B_u , which are 32 in this case
- 9: **for** k=1 to col **do**
- 10: $dark = DC(B_u)$ $\triangleright DC$ is dark channel
- 11: **end for**
- 12: **end for**
- 13: Select the top $h\%$ brightest pixels from $dark$ $\triangleright h$ is taken as 1%
- 14: $A = \text{median}(B_u(h))$

The informed reader would notice that our algorithm differs from the main stream of state-of-the-art algorithms which rather operate with segmenting an image into two regions namely, sky and non-sky regions, then extracting the atmospheric light from the sky region. Our proposed method does not segment an image into the above-mentioned two regions explicitly. Instead of considering a segmentation algorithm for dividing an image into two regions, we apply Algorithm 2 to compute atmospheric light. Algorithm 2 divides an image into several equal-sized blocks and then atmospheric light is calculated from a

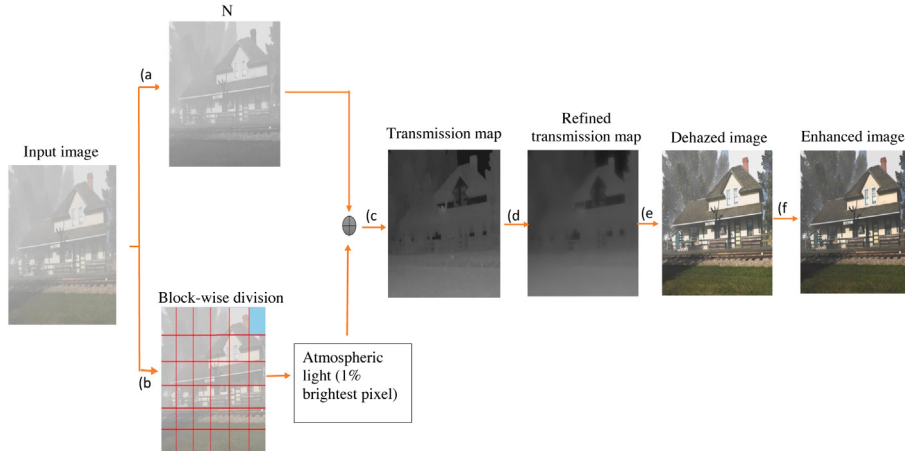


Fig. 2. Different steps involved in the proposed method are (a) Image in N channel, (b) Calculation of atmospheric light, (c) Generation of transmission map, (d) Refinement of transmission map, (e) Dehazed image and (f) Enhancement of dehazed image.

B1	B2	B3	B4	B5	B6	B7	B8
B9	B10	B11	B12	B13	B14	B15	B16
B17	B18	B19	B20	B21	B22	B23	B24
B25	B26	B27	B28	B29	B30	B31	B32
B33	B34	B35	B36	B37	B38	B39	B40
B41	B42	B43	B44	B45	B46	B47	B48
B49	B50	B51	B52	B53	B54	B55	B56
B57	B58	B59	B60	B61	B62	B63	B64

Fig. 3. Selection of a block having the maximum score, Max . Here, the box marked by green color indicates the candidate block, B_u .

block, which is selected based on statistical features namely, mean and standard deviation. We thus did not opt for a segmentation phase using for instance grab cut explicitly because not only it incurs an additional computational cost but it also does not necessarily improve the results. We have tested indeed two very recent methods for extracting the atmospheric light involving the grab cut segmentation algorithm [54,55]. However, these results are not included in the manuscript because, in most cases, the grab cut algorithm fails to separate the sky region from an image. On the other hand, the proposed Algorithm 2 computes atmospheric light from the sky region in most of the cases. Nevertheless, sometimes Algorithm 2 fails especially when images are captured in indoor conditions.

3.2. Transmission map

In almost every DCP based methods, transmission map is calculated using Eq. (9).

$$t(m) = 1 - \omega \min_{c \in \{R, G, B\}} \left(\min_p \frac{I^c(p)}{A^c} \right), \quad (9)$$

where c is a particular color channel of I , p is a local patch centered at m , ω ($0 < \omega \leq 1$) is a constant used to preserve a small amount of haze in image. However, the value estimated using Eq. (9) is not accurate always. Therefore, a new color channel, N , is adopted to calculate the transmission map. The motivation behind the use of a new color channel is as follows. It is observed that illumination present in the sky region of an image is not uniform or homogeneous and it happens due to the difference in atmospheric scattering angles. Moreover, the inhomogeneous brightness distribution of an image, especially the sky region, creates a serious issue while estimating the transmission map. So, a relatively new color channel is adopted to the removal of atmospheric scattering. The new channel is computed using Eq. (10) [56].

$$N = \phi - (\alpha - \beta), \quad (10)$$

where ϕ is known as the panchromatic channel and it refers to the channel which is sensitive to all visible colors. In other words, ϕ is also called gray-scale image obtained by $\phi = 0.299R + 0.587G + 0.114B$, where R, G, B are the red, green, and blue channels of an RGB color image,

Table 1
Value of score corresponding to each block of Fig. 3.

		Blocks							
Score		0.7780	0.8053	0.7898	0.7326	0.7705	0.7427	0.7220	0.6336
		0.3157	0.5389	0.6266	0.6092	0.6476	0.5797	0.5631	0.4532
		0.1767	0.3073	0.4157	0.4168	0.3828	0.4424	0.4021	0.3935
		0.2004	0.2600	0.3133	0.3136	0.2493	0.3450	0.3506	0.3647
		0.1853	0.2371	0.2709	0.2812	0.1943	0.2438	0.3169	0.2628
		0.1673	0.1554	0.1895	0.1983	0.2085	0.2376	0.2319	0.1859
		0.2679	0.1993	0.1907	0.1882	0.1567	0.2399	0.2034	0.1642
		0.2234	0.2360	0.2333	0.1747	0.1681	0.2077	0.1964	0.1856

Table 2

Comparison of the RMSE value between the ground truth and the estimated atmospheric light of the ten images taken from FRIDA dataset [44].

Images	M1 [19]	M2 [48]	M3 [49]	M4 [50]	M5 [47]	M6 [46]	M7 [26]	M8 [33]	M10 [24]	M11 [45]	M12
img1	0.0350 ⁽²⁾	0.7480	0.0649	0.0651	0.0379 ⁽³⁾	0.0350 ⁽²⁾	0.0757	0.7478	0.0523	0.0350 ⁽²⁾	0.0348⁽¹⁾
img2	0.0406 ⁽²⁾	0.7480	0.0913	0.0466	0.0608	0.0407 ⁽³⁾	0.0863	0.7477	0.0560	0.0406 ⁽²⁾	0.0402⁽¹⁾
img3	0.0478 ⁽²⁾	0.7847	0.0874	0.0851	0.0638	0.0479 ⁽³⁾	0.0874	0.7847	0.0614	0.0478 ⁽²⁾	0.0473⁽¹⁾
img4	0.0482 ⁽²⁾	0.7847	0.0739	0.0869	0.0489	0.0482 ⁽²⁾	0.0482 ⁽²⁾	0.7847	0.0488 ⁽³⁾	0.0482 ⁽²⁾	0.0478⁽¹⁾
img5	0.0401 ⁽²⁾	0.8353	0.0606	0.1164	0.0406	0.0401 ⁽²⁾	0.0401 ⁽²⁾	0.8353	0.0405 ⁽³⁾	0.0401 ⁽²⁾	0.0400⁽¹⁾
img6	0.0398 ⁽²⁾	0.8353	0.0771	0.1167	0.0431 ⁽³⁾	0.0398 ⁽²⁾	0.0398 ⁽²⁾	0.8353	0.0431	0.0398 ⁽²⁾	0.0395⁽¹⁾
img7	0.0151 ⁽³⁾	0.8466	0.0341	0.0122⁽¹⁾	0.0152	0.0151 ⁽³⁾	0.0151 ⁽³⁾	0.8464	0.0155	0.0151 ⁽³⁾	0.0150 ⁽²⁾
img8	0.0151 ⁽³⁾	0.8466	0.0224	0.0122⁽¹⁾	0.0151 ⁽³⁾	0.0151 ⁽³⁾	0.0151 ⁽³⁾	0.8464	0.0151 ⁽³⁾	0.0151 ⁽³⁾	0.0148 ⁽²⁾
img9	0.0172 ⁽³⁾	0.8466	0.0172 ⁽³⁾	0.0144⁽¹⁾	0.0172 ⁽³⁾	0.0172 ⁽³⁾	0.0172 ⁽³⁾	0.8464	0.0173	0.0172 ⁽³⁾	0.0171 ⁽²⁾
img10	0.0339 ⁽²⁾	0.9143	0.0407	0.0660	0.0339 ⁽²⁾	0.0339 ⁽²⁾	0.0339 ⁽²⁾	0.9141	0.0341 ⁽³⁾	0.0339 ⁽²⁾	0.0337⁽¹⁾

Table 3

Names of the ten images taken from RESIDE dataset [43] and their estimated RMSE values by various methods.

Images	M1 [19]	M2 [48]	M3 [49]	M4 [50]	M5 [47]	M6 [46]	M7 [26]	M8 [33]	M10 [24]	M11 [45]	M12
img11	0.3949 ⁽²⁾	0.7777	0.8257	0.6803	0.7189	0.6594 ⁽³⁾	0.6674	0.7515	0.6983	0.8795	0.1851⁽¹⁾
img12	0.5509 ⁽²⁾	0.7643	0.8097	0.6713	0.7081	0.6553	0.6155 ⁽³⁾	0.7093	0.6906	0.8588	0.3812⁽¹⁾
img13	0.9784	0.0690	0.0977	0.0908	0.0528 ⁽²⁾	0.0362⁽¹⁾	0.1562	0.0632	0.0552 ⁽³⁾	0.2011	0.6530
img14	0.4840 ⁽²⁾	0.8004	0.8550	0.7069	0.7403	0.6747 ⁽³⁾	0.7216	0.7361	0.7176	0.9044	0.2963⁽¹⁾
img15	0.6670 ⁽²⁾	0.7722	0.7756	0.7320	0.7449	0.7307 ⁽³⁾	0.7687	0.7647	0.7614	0.7828	0.3371⁽¹⁾
img16	0.7456	0.6855	0.7333	0.5649	0.6304	0.5611	0.4443 ⁽³⁾	0.5747	0.6028	0.4335 ⁽²⁾	0.3051⁽¹⁾
img17	0.9789	0.0913	0.1211	0.0699	0.0702	0.0490 ⁽²⁾	0.1651	0.0730	0.0515 ⁽³⁾	0.2041	0.0283⁽¹⁾
img18	0.9784	0.0751	0.1028	0.0720	0.0579	0.0411 ⁽³⁾	0.1058	0.0476	0.0378 ⁽²⁾	0.2064	0.0149⁽¹⁾
img19	0.9784	0.0951	0.1217	0.0795	0.0721	0.0526 ⁽²⁾	0.4607	0.0711	0.0552 ⁽³⁾	0.2064	0.0258⁽¹⁾
img20	0.9784	0.0786	0.1087	0.0890	0.0589	0.0419 ⁽²⁾	0.4327	0.0546	0.0475 ⁽³⁾	0.2059	0.0103⁽¹⁾

respectively. The $\alpha = \max\{R, G, B\}$ is called the bright channel and it denotes the maximum value of each pixel in an RGB color image. The $\beta = \min\{R, G, B\}$ is known as the dark channel and it represents the channel of the minimum value of each pixel in a RGB color image. In general, the blue and red channels are the bright and the dark channels respectively for most of the images with the sky regions. The difference between the blue and red channels represents the deviation of the atmospheric scattering of each pixel in the visible range, which can be considered as the atmospheric background for estimating the transmission map in this study. The modified equation to compute the transmission map is shown in Eq. (11). An experiment is performed to prove the correctness of Eq. (11), which will be discussed in Section 4.

$$t(m) = 1 - \omega \min_p \left(\frac{N(p)}{A} \right), \quad (11)$$

where ω and p are taken as 0.85 and 15, respectively. The coarse transmission map calculated using Eq. (11) suffers from block artifacts and halo effects because transmission is not always constant in the patch. Therefore, filters are used to refine the transmission in order to remove noise. Several filters, for example, bilateral filter, gaussian filter, soft matting, cross-bilateral filter, and guided filter were considered for the refinement. One of the previous studies [57] revealed that soft matting, cross-bilateral filter, and guided filter provide sharper transmission maps than gaussian and bilateral filters. Moreover, Lee [57] proved that the soft matting performed the best, and the cross-bilateral and guided filters stood in second. However, the time complexity of the

guided filter is low as compared to others. The complexity is expressed as $O(N)$, where N is the total number of pixel of I [58]. Moreover, a guided filter performs edge-preserving smoothing operation on I using the information of the guidance image. Further, it does not suffer from the gradient reversal artifacts that can be observed while using bilateral filter. The output image, \hat{I} , can be represented as a linear combination of the guidance image, I , in a guided filter. Here, the guided filter is used to optimize the transmission map as shown in Eq. (12).

$$\hat{I}_i = a_m I_i + b_m, \quad \forall i \in w_m, \quad (12)$$

where a_m and b_m are two constants in window w_m centered at pixel m . The value of a_m and b_m are obtained by Eqs. (13) and (14), respectively.

$$a_m = \frac{\frac{1}{|w|} \sum_{i \in w_m} I_i t_i - \mu_m t'_m}{\sigma_m^2 + \epsilon}, \quad (13)$$

$$b_m = t'_m - a_m \mu_m, \quad (14)$$

where t is the coarse transmission map, σ_m^2 is the variance, μ_m is the mean of I , $t' = \frac{1}{|w|} \sum_{i \in w_m} t_i$, and $|w|$ is the total number of pixels in filter w_m .

3.3. Radiance

After calculating A and t using the above said methods, the radiance of an image is recovered by the Eq. (1). However, the direct attenuation



Fig. 4. Illustration of results of atmospheric light estimation algorithm. Red box indicates the selected block.

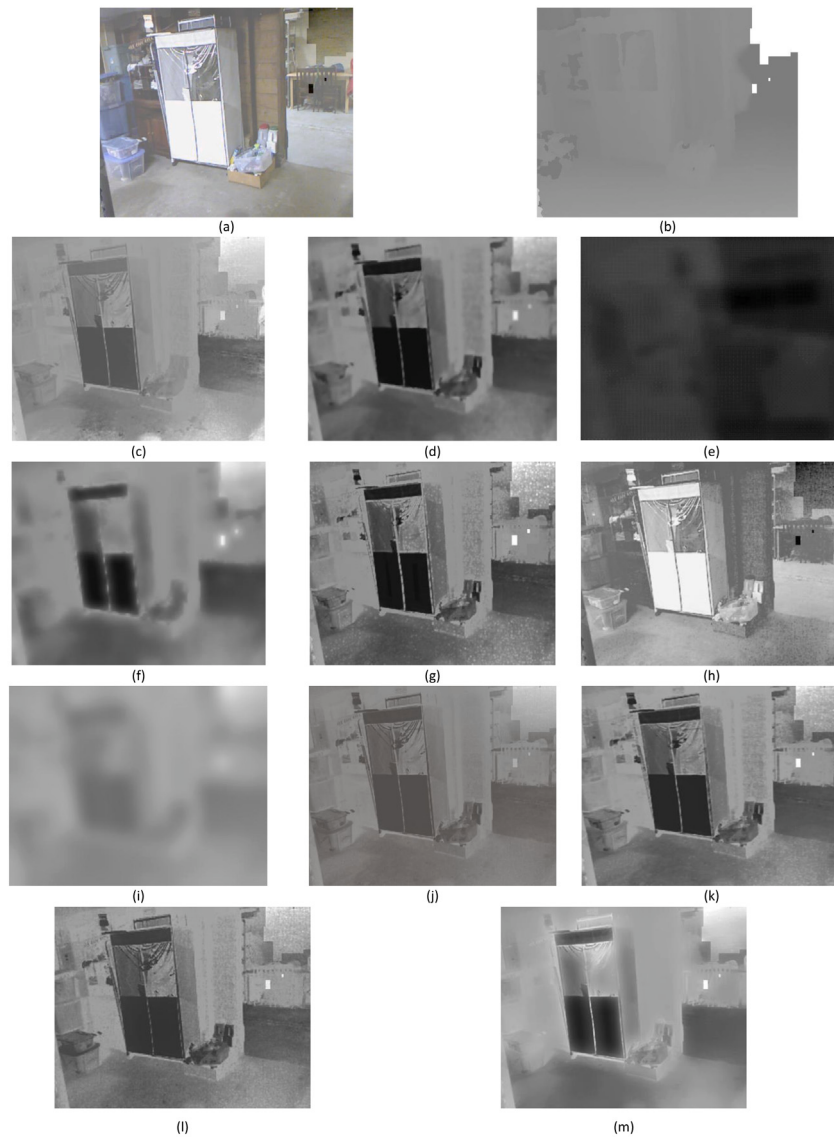


Fig. 5. (a) A sample image, ‘img11’, of RESIDE [43] dataset, (b) given transmission map, obtained transmission maps by, (c) M1 [19], (d) M2 [48], (e) M3 [49], (f) M4 [50], (g) M5 [47], (h) M6 [46], (i) M7 [26], (j) M8 [33], (k) M10 [24], (l) M11 [45] and (m) M12.

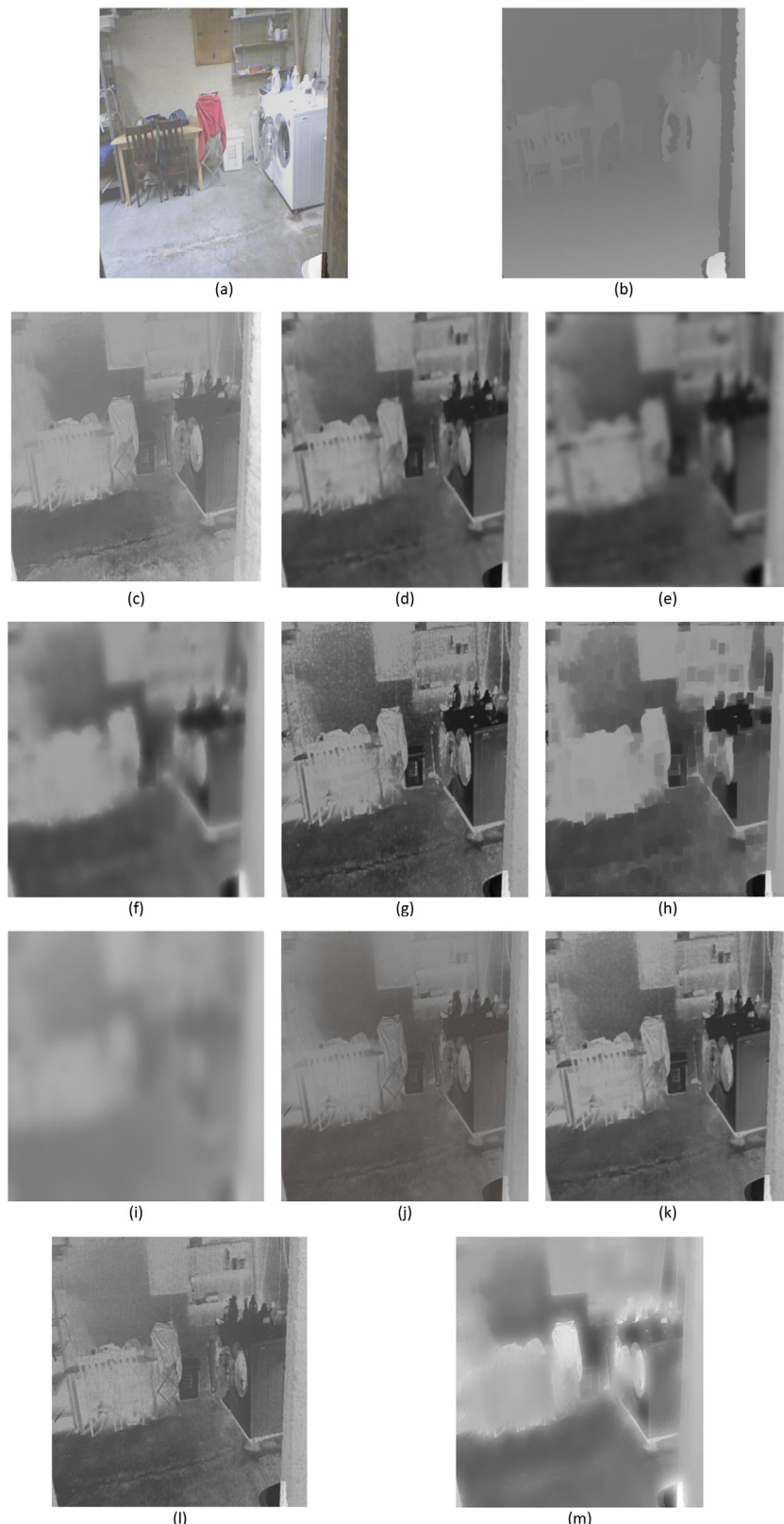


Fig. 6. (a) A sample image, ‘img12’, of RESIDE [43] dataset, (b) given transmission map, obtained transmission maps by (c) M1 [19], (d) M2 [48], (e) M3 [49], (f) M4 [50], (g) M5 [47], (h) M6 [46], (i) M7 [26], (j) M8 [33], (k) M10 [24], (l) M11 [45] and (m) M12.

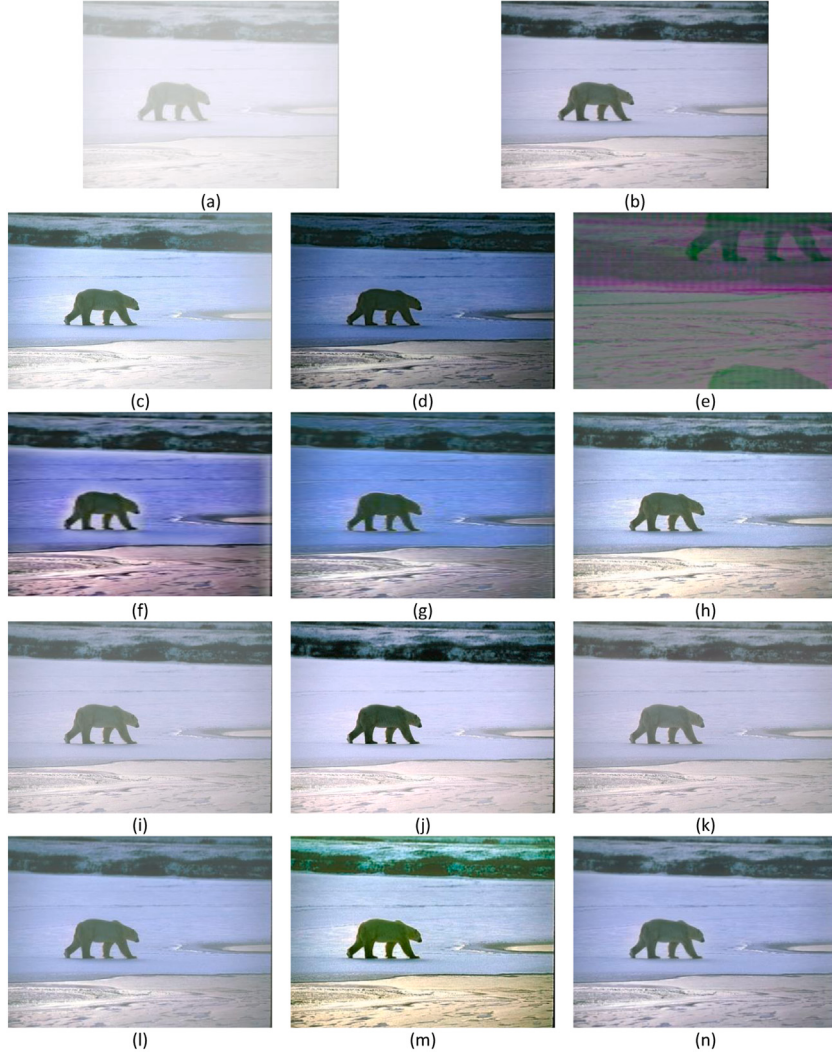


Fig. 7. Image dehazing results of twelve different methods on BSDS500 [42] dataset, (a) hazy image, (b) ground truth image, output of (c) M1 [19], (d) M2 [48], (e) M3 [49], (f) M4 [50], (g) M5 [47], (h) M6 [46], (i) M7 [26], (j) M8 [33], (k) M9 [34], (l) M10 [24], (m) M11 [45] and (n) M12.

term $J(m)t(m)$ may be close to zero when the transmission $t(m)$ is close to zero [29]. Therefore, the transmission map is restricted by a constant t_0 . Finally, the scene radiance $J(m)$ is recovered using Eq. (15).

$$J(m) = \frac{I^c(m) - A^c}{\max(\hat{t}(m), t_0)} + A^c, \quad (15)$$

here value of t_0 is taken as 0.1.

3.4. Enhancement

After the restoration of radiance, it is being observed that an image becomes either too bright or too dark. Therefore, to improve the visibility of the image, adjustment of illuminance is required. Illuminance scaling factor [25] is used to adjust the illumination of the image, which is calculated using Eq. (16).

$$s(m) = \frac{Y_{J(m)}Y_{I(m)} + \tau Y_{I(m)}^{1.5}}{Y_{J(m)}^3 + \tau Y_{I(m)}^{1.5}}, \quad (16)$$

where $s(m)$ is the illuminance scaling factor, Y_J is the illumination intensity of the dehazed image, Y_I is the illumination intensity of the input image, τ is a constant taken as 1.2. Thus, the enhanced image can

be obtained by using Eq. (17):

$$E(m) = J^c(m) * s(m), \quad (17)$$

where E is the enhanced haze-free image. All the steps of the proposed method are written in the form of an Algorithm 3.

Algorithm 3 Removal of haze

Input: Hazy Image I and atmospheric light A

Output: Enhanced Image, E

- 1: Find N , $N = \phi - (\alpha - \beta)$
 - 2: Calculate A using Algorithm 2
 - 3: **for** all pixels m , **do**
 - 4: Estimate transmission, $t(m) = 1 - \omega \min_p(\frac{N(p)}{A})$
 - 5: **end for**
 - 6: Refine transmission map using guided filter
 - 7: Compute radiance, $J(m) = \frac{I^c(m) - A^c}{\max(t(m), t_0)} + A^c$
 - 8: **for** all pixels m , **do**
 - 9: Calculate illuminance scaling factor, $s(m) = \frac{Y_{J(m)}Y_{I(m)} + \tau Y_{I(m)}^{1.5}}{Y_{J(m)}^3 + \tau Y_{I(m)}^{1.5}}$
 - 10: **end for**
 - 11: Enhanced image, $E(m) = J^c(m) * s(m)$
-

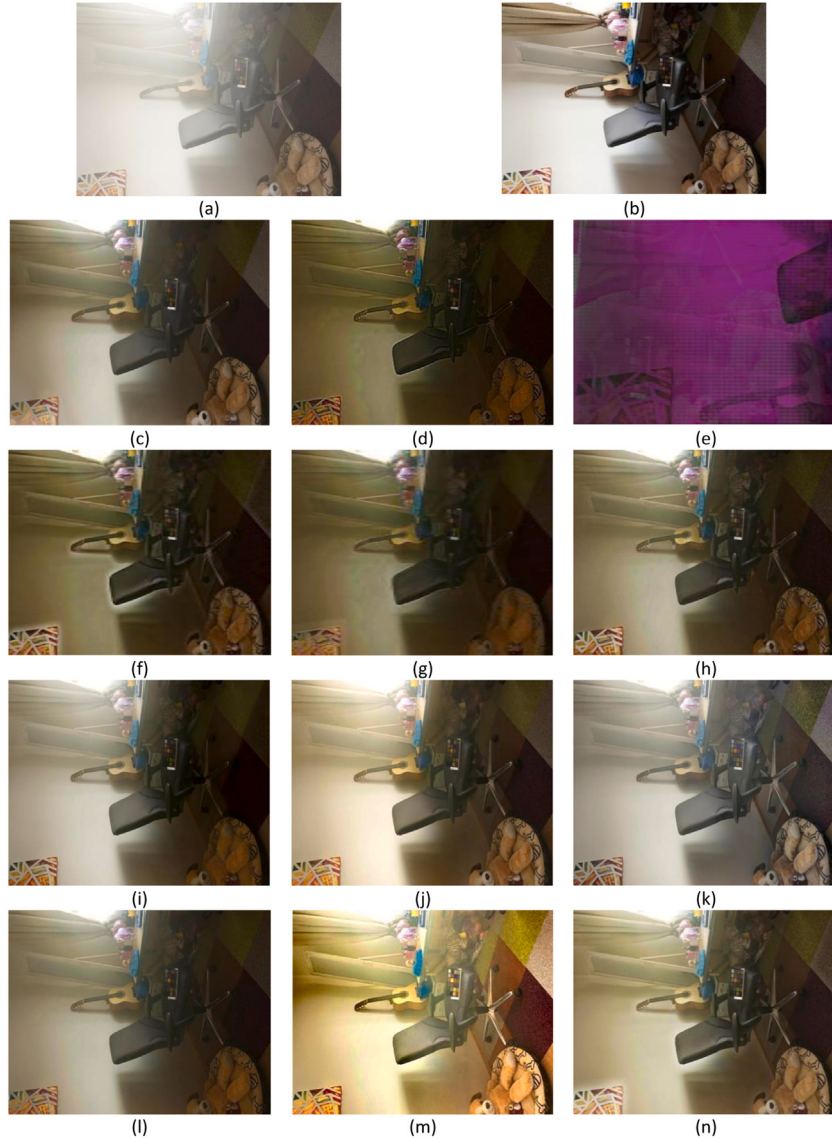


Fig. 8. Image dehazing results of twelve different methods on I-HAZE [41] dataset, (a) hazy image, (b) ground truth image, output of (c) M1 [19], (d) M2 [48], (e) M3 [49], (f) M4 [50], (g) M5 [47], (h) M6 [46], (i) M7 [26], (j) M8 [33], (k) M9 [34], (l) M10 [24], (m) M11 [45] and (n) M12.

4. Experimental results and discussion

All the experiments are performed in MATLAB R2018a using a PC having Intel(R) Core™ i7-4770 CPU @ 3.40 GHz and 4 GB RAM.

4.1. Database description

To evaluate the performance of the proposed method, six datasets namely, O-HAZE, I-HAZE, BSDS500, RESIDE, FRIDA, and natural hazy images from Google, are used. The reason behind including many datasets is to compare the performance on various environmental conditions. The O-HAZE dataset consists of 45 outdoor scene pairs of real hazy and corresponding haze-free images. The I-HAZE dataset contains 35 pairs of hazy and corresponding haze-free indoor images. All the hazy images were captured in a real hazy environment generated by professional haze machines maintaining the same value of illumination parameters. The BSDS500 consists of 500 natural images. All the images are clear; there is no haze present in them. One hundred and twenty-five images are selected randomly from BSDS500 and synthetic haze is introduced to make corresponding hazy images. Besides this, RESIDE dataset is also considered to compare the transmission map

estimated by the proposed method with other state-of-the-art methods for knowing which method determines a transmission map close to the actual. It consists of real and synthetic hazy images along with their transmission maps. So, we compare all the methods based on the produced transmission maps. The FRIDA dataset is considered to validate the atmospheric light estimation algorithm. The FRIDA dataset consists of 90 synthetic images of 18 urban road scenes. Each fog-free image is associated with four foggy images and a depth map. Different kinds of fog are added on each of the 4 associated images namely, uniform fog, heterogeneous fog, cloudy fog, and cloudy heterogeneous fog.

4.2. Computational protocols

Based on the qualitative evaluation, quantitative evaluation, and execution time, the performance of the proposed method is compared with eleven state-of-the-art methods, which are as follows:

- M1: Single image haze removal using DCP [19]
- M2: Fast image dehazing using guided joint bilateral filter [48]



Fig. 9. Image dehazing results of twelve different methods on O-HAZE [40] dataset, (a) hazy image, (b) ground truth image, output of (c) M1 [19], (d) M2 [48], (e) M3 [49], (f) M4 [50], (g) M5 [47], (h) M6 [46], (i) M7 [26], (j) M8 [33], (k) M9 [34], (l) M10 [24], (m) M11 [45] and (n) M12.

- M3: Fast haze removal for a single remote sensing image using DCP [49]
- M4: Dehazing for image and video using guided filter [50]
- M5: Visibility enhancement of single hazy images using hybrid DCP [47]
- M6: Fast single-image defogging [46]
- M7: A fast single image haze removal algorithm using color attenuation prior [26]
- M8: Haze removal method for natural restoration of images with sky [33]
- M9: Image dehazing by artificial multiple-exposure image fusion [34]
- M10: Efficient single image dehazing by modifying the DCP [24]
- M11: Multi-scale optimal fusion model for single image dehazing [45]
- M12: The proposed method

4.3. Results and comparison

Three experiments are mainly conducted in this study. The aim of the first experiment is to know how good *M12* is as compared to *M1–M11* while estimating atmospheric light. Here, Fig. 3 is again considered. The score of each B_i is calculated using Algorithm 2 and is tabulated in Table 1. The block, B_u , having the highest score, Max , is

highlighted by green color in Fig. 3. The highest score is also marked by bold character in Table 1. Moreover, Fig. 4 shows the region bounded by a rectangle, indicating the block used for estimation of atmospheric light, A . It can be observed that the candidate block, B_u , is selected from the sky region. Further, FRIDA dataset is used for objective analysis. The fog-free images and their respective depth maps are taken from the FRIDA dataset. A foggy image is formed using Eq. (1). However, the value of atmospheric light is provided manually as an input to create a foggy image. Then, algorithm 2 is employed to calculate an atmospheric light. An evaluation metric named root means square error (RMSE) [59] is considered, which computes the value of the RMSE between the input and the estimated atmospheric lights. The ideal value of the RMSE is 0. Table 2 reports the values of the RMSE obtained by *M1–M12* except *M9* for ten randomly chosen sample images from the FRIDA dataset. A rank either 1st or 2nd or 3rd is assigned to each method for each image, which is enclosed within the bracket. It is clear from Table 2 that the *M12* stands the 1st for most of the images since the values of the RMSE are less as compared to other state-of-the-art methods. However, *M4* estimates the atmospheric light better than others for some images. All the results of Table 2 illustrate that the *M12* is more consistent while estimating an atmospheric light from a foggy image, which shows the effectiveness of the *M12* over *M1–M11*.

The objective of the second experiment is to determine which method estimates the transmission map better than others. So, the

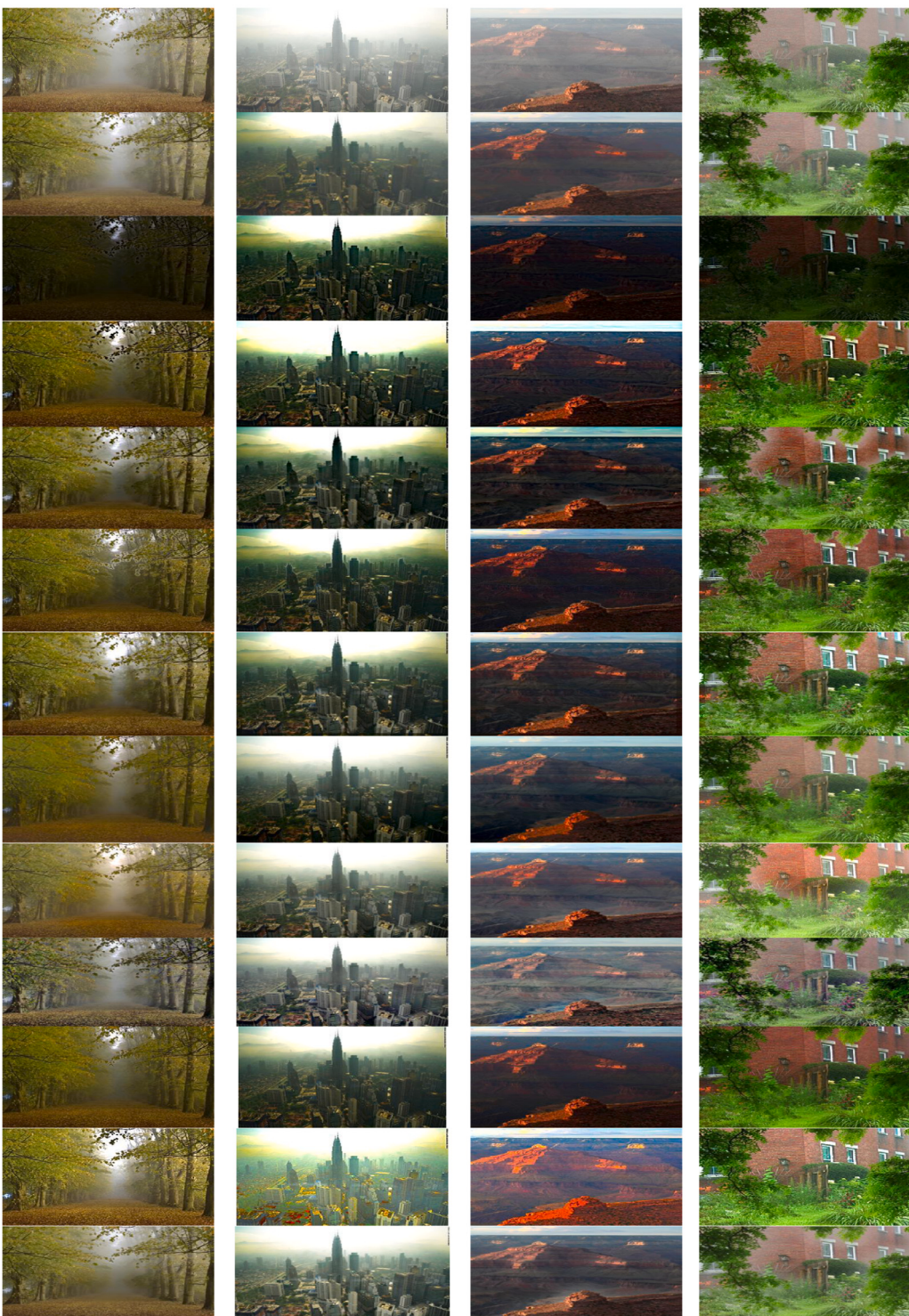


Fig. 10. Image dehazing results of twelve different methods on natural hazy images taken from Google, from top to bottom rows: original images, output of M1 [19], M2 [48], M3 [49], M4 [50], M5 [47], M6 [46], M7 [26], M8 [33], M9 [34], M10 [24], M11 [45] and M12.

RESIDE dataset is considered only because it has synthetic hazy images and their transmission maps. Ten images are considered randomly from the RESIDE dataset for this experiment. However, the transmission maps obtained by all the methods except *M9* on two synthetic hazy images namely, ‘img11’ and ‘img12’ including themselves are shown in Figs. 5 and 6 respectively. Since *M9* does not estimate an atmospheric light and transmission map, it is not considered in the first two experiments. It is clear from both Figs. 5 and 6 that the visual quality of the transmission map obtained by the *M12* is better than the transmission

maps generated by *M1–M11* methods. Hence, the *M12* outperforms the other eleven state-of-the-art methods, *M1–M11*. However, the visual quality is measured by the human visual system (HVS) and it may vary from person to person. Thus, it is not a unique and sufficient criterion. So, quantitative evaluation is required. Again the RMSE is adopted. Now, the value of RMSE is obtained between the given transmission map and the transmission map obtained by *M1 – M12* except for the *M9* on 10 randomly selected images from the RESIDE dataset and the achieved values of the RMSE are noted in Table 3. Again a rank is

Table 4

The average values of fourteen quantitative evaluation metrics on BSDS500 [42] dataset.

Dataset	Metrics	M1 [19]	M2 [48]	M3 [49]	M4 [50]	M5 [47]	M6 [46]	M7 [26]	M8 [33]	M9 [34]	M10 [24]	M11 [45]	M12
BSDS500	SSIM	0.0041 ⁽³⁾	0.0015	0.0022	0.0020	0.0018	0.0022	0.0027	0.9445 ⁽²⁾	0.0026	0.0021	0.0031	0.9608⁽¹⁾
	PSNR	6.6111 ⁽³⁾	6.5719	6.6033	6.5918	6.5855	6.6012	6.0331	22.216 ⁽²⁾	6.0991	6.5982	6.6060	49.859⁽¹⁾
	MSE	15667.5	15785.2	15685.6	15725.2	15747.4	15698.7	15209.4 ⁽³⁾	390.32 ⁽²⁾	15837.7	15701.1	15685.1	104.37⁽¹⁾
	RMSE	122.09 ⁽³⁾	122.59	122.18	122.38	122.28	122.22	178.46	19.75 ⁽²⁾	125.31	122.25	122.16	3.230⁽¹⁾
	GMSD	0.00024 ⁽²⁾	0.000501	0.00047	0.00046	0.00043	0.00035	0.00016	0.35735	0.00018	0.00029 ⁽³⁾	0.00042	0.00002⁽¹⁾
	BIAS	0.9939 ⁽³⁾	0.9971	0.9944	0.9958	0.9947	0.9950	0.9957	0.0661 ⁽²⁾	0.9959	0.9951	0.9943	0.0202⁽¹⁾
	FSIM	0.4773	0.4550	0.4619	0.4743	0.4616	0.4744	0.5092 ⁽³⁾	0.9526 ⁽²⁾	0.5089	0.4691	0.4668	0.9973⁽¹⁾
	FSIMc	0.4628	0.4417	0.4482	0.4604	0.4480	0.4606	0.5024 ⁽³⁾	0.9515 ⁽²⁾	0.5020	0.4552	0.4530	0.9973⁽¹⁾
	RFSIM	0.9345	0.9517	0.9547 ⁽³⁾	0.9123	0.9255	0.9354	0.9704⁽¹⁾	0.0004	0.9698 ⁽²⁾	0.9448	0.8942	0.0049
	ERGAS	112.926	113.236	112.917	113.100	112.883	113.013	103.85 ⁽³⁾	11.487 ⁽²⁾	103.87	113.040	112.935	21.801⁽¹⁾
	BRISQUE	17.307 ⁽²⁾	22.136	22.145	24.512	30.169	24.514	23.142	24.6805	20.629	17.049⁽¹⁾	33.586	20.585 ⁽³⁾
	NIQE	3.458 ⁽²⁾	4.051	4.125	3.552	5.191	3.769	4.200	3.590	3.518	3.468 ⁽³⁾	4.958	3.451⁽¹⁾
	CEIQ	2.422	2.635 ⁽²⁾	1.402	1.402	2.603	2.574	1.402	2.382	2.285	2.377	2.728⁽¹⁾	2.608 ⁽³⁾
	E	0	6.7566	6.9070 ⁽³⁾	0	6.9708 ⁽²⁾	7.0661	0	0	6.7346	6.7789	7.3780⁽¹⁾	6.8592

Table 5

The average values of fourteen quantitative evaluation metrics on I-HAZE [41] dataset.

Dataset	Metrics	M1 [19]	M2 [48]	M3 [49]	M4 [50]	M5 [47]	M6 [46]	M7 [26]	M8 [33]	M9 [34]	M10 [24]	M11 [45]	M12
I-HAZE	SSIM	0.0043	0.0030	0.0032	0.0031	0.0031	0.0036	0.0058	0.5739⁽¹⁾	0.0061 ⁽³⁾	0.0033	0.0049	0.5342 ⁽²⁾
	PSNR	5.8343	5.8084	5.8142	5.8115	5.8128	5.8230	6.9557	12.6206⁽²⁾	6.9634 ⁽³⁾	5.8145	5.8418	15.840⁽¹⁾
	MSE	17003.9	17105.9	17082.2	17093.4	17087.9	17048.1	13728.6	3556.4 ⁽²⁾	13708.6 ⁽³⁾	17072.3	16975.1	6981.2⁽¹⁾
	RMSE	130.33	130.72	130.63	130.67	130.65	130.50	115.89	59.635⁽¹⁾	115.80 ⁽³⁾	130.59	130.22	90.239 ⁽²⁾
	GMSD	0.00026⁽¹⁾	0.00051	0.00049	0.00044	0.00044	0.00039	0.00038 ⁽³⁾	0.2752	0.00028 ⁽²⁾	0.00038	0.00044	0.00043
	BIAS	0.9962	0.9990	0.9980	0.9982	0.9972	0.9296 ⁽³⁾	0.3271 ⁽²⁾	0.9958	0.9975	0.9962	0.9962	0.1348⁽¹⁾
	FSIM	0.5731	0.5431	0.5288	0.5405	0.5556	0.5565	0.5835 ⁽³⁾	0.8596⁽¹⁾	0.5289	0.5622	0.5614	0.8474 ⁽²⁾
	FSIMc	0.5663	0.5364	0.5223	0.5340	0.5506	0.5498	0.5775 ⁽³⁾	0.8509⁽¹⁾	0.5193	0.5553	0.5402	0.8505 ⁽²⁾
	RFSIM	0.9485	0.9730 ⁽²⁾	0.9938⁽¹⁾	0.9583	0.9385	0.9167	0.9296	0.0005	0.9560	0.9379	0.8827	0.9605 ⁽³⁾
	ERGAS	114.722 ⁽³⁾	114.993	114.889	114.914	114.841	114.805	117.089	51.992⁽¹⁾	116.996	114.845	114.694	74.422 ⁽²⁾
	BRISQUE	29.983	15.226 ⁽²⁾	28.435	26.743	9.714⁽¹⁾	18.059	19.237	28.598	25.179	26.477	17.797	16.520 ⁽³⁾
	NIQE	3.225	3.535	3.423	3.902	4.092	3.375	4.127	3.102 ⁽³⁾	3.254	3.354	2.457⁽¹⁾	2.990 ⁽²⁾
	CEIQ	2.373	2.309	1.402	1.402	2.282	2.429	1.402	2.600	2.631 ⁽²⁾	2.505	2.762⁽¹⁾	2.608 ⁽³⁾
	E	0.6828	5.9665	6.8917	0	6.3748	6.7219	0	0	6.9630 ⁽²⁾	6.5706	6.9234 ⁽³⁾	7.2362⁽¹⁾

Table 6

The average values of fourteen quantitative evaluation metrics on O-HAZE [40] dataset.

Dataset	Metrics	M1 [19]	M2 [48]	M3 [49]	M4 [50]	M5 [47]	M6 [46]	M7 [26]	M8 [33]	M9 [34]	M10 [24]	M11 [45]	M12
O-HAZE	SSIM	0.0027	0.0008	0.0012	0.0013	0.0014	0.0017	0.0019	0.3456 ⁽²⁾	0.0017	0.0017	0.0028 ⁽³⁾	0.9643⁽¹⁾
	PSNR	7.3819	7.3551	7.3622	7.3652	7.3617	7.3639	7.3852	7.3697	8.3101 ⁽³⁾	8.2685	8.3103 ⁽²⁾	52.407⁽¹⁾
	MSE	11886.1	11919.4	10305.2	9687.7 ⁽²⁾	10306.9 ⁽³⁾	11935.1	11876.9	11959.2	11939.7	11931.3	11941.1	3734.9⁽¹⁾
	RMSE	109.01	109.34	109.26	109.22	109.26	109.16	99.797 ⁽³⁾	98.42 ⁽²⁾	99.802	109.239	108.972	61.114⁽¹⁾
	GMSD	0.00026 ⁽²⁾	0.00057	0.00057	0.00046	0.00047	0.00047	0.00033	0.30609	0.00029 ⁽³⁾	0.00042	0.00041	0.0004⁽¹⁾
	BIAS	0.9955 ⁽³⁾	0.9989	0.9977	0.9972	0.9975	0.9967	0.9960	0.7084 ⁽²⁾	0.9955	0.9971	0.9955	0.6197⁽¹⁾
	FSIM	0.3220	0.2981	0.3005	0.3143	0.3159	0.3144	0.3648	0.7632 ⁽²⁾	0.3666 ⁽³⁾	0.3151	0.3222	0.9694⁽¹⁾
	FSIMc	0.3182 ⁽²⁾	0.2945	0.2971	0.3105	0.3143	0.3107	0.3690	0.7923 ⁽²⁾	0.3707 ⁽³⁾	0.3113	0.3186	0.9694⁽¹⁾
	RFSIM	0.9707	0.9707 ⁽³⁾	0.9773⁽²⁾	0.9552	0.9449	0.9436	0.9613	0.00049	0.9774⁽¹⁾	0.9519	0.9440	0.9638
	ERGAS	108.023 ⁽³⁾	108.349	108.224	108.183	108.213	108.125	109.90	70.775 ⁽²⁾	109.86	108.172	108.003	52.446⁽¹⁾
	BRISQUE	24.992	21.426	23.532	24.501	23.507	14.999 ⁽²⁾	21.847	17.243 ⁽³⁾	18.147	14.326⁽¹⁾	19.675	23.719
	NIQE	2.327⁽¹⁾	2.439	2.549	2.684	3.529	2.442	2.537	2.683	2.651	2.561	3.345 ⁽²⁾	2.396 ⁽³⁾
	CEIQ	2.545	2.236	1.402	1.402	2.420	2.581	1.402	2.631 ⁽²⁾	2.388	2.530	2.643⁽¹⁾	2.588 ⁽³⁾
	E	0.7666	6.7620	6.9888	0	6.6064	6.9411 ⁽³⁾	0.0009	0	6.6141	6.6884	7.3901⁽¹⁾	6.9545 ⁽²⁾

Table 7

The average values of four no-reference quantitative evaluation metrics on natural hazy images shown in Fig. 10.

Metrics	Image	M1 [19]	M2 [48]	M3 [49]	M4 [50]	M5 [47]	M6 [46]	M7 [26]	M8 [33]	M9 [34]	M10 [24]	M11 [45]	M12
BRISQUE	img1	21.991	6.067 ⁽²⁾	17.447	15.825	24.229	13.952	10.479	11.931	5.002⁽¹⁾	15.824	28.630	9.516 ⁽³⁾
	img2	15.612 ⁽²⁾	12.748⁽¹⁾	35.236	45.729	29.801	28.337	44.412	21.716	42.723	24.326	35.763	21.639 ⁽³⁾
	img3	36.377	31.600	28.497	36.137	19.160 ⁽²⁾	35.174	44.429	35.151	9.751⁽¹⁾	37.616	28.487 ⁽³⁾	41.708
	img4	21.232⁽¹⁾	36.399	33.358	44.654	39.845	32.835	42.821	29.289 ⁽²⁾	32.775	31.389	38.913	31.342 ⁽³⁾
NIEQ	img1	2.417 ⁽²⁾	2.601	2.754	2.645	3.970	2.665	3.102	2.562 ⁽³⁾	2.650	4.041	4.507	2.375⁽¹⁾
	img2	3.133	2.507⁽¹⁾	3.126	10.515	2.978 ⁽²⁾	3.204	12.346	3.095	4.293	3.564	4.212	3.090 ⁽³⁾
	img3	3.730 ⁽²⁾	3.477⁽¹⁾	4.511	3.872	6.032	3.888	4.634	3.748 ⁽³⁾	5.056	4.835	5.962	3.953
	img4	5.487⁽¹⁾	7.031	12.463	7.064	8.684	6.509	6.134 ⁽²⁾	9.322	6.535	7.628	9.433	6.194 ⁽³⁾
CEIQ	img1	2.456	1.915	2.459	1.402	2.270	2.435	1.402	2.462	2.548 ⁽³⁾	2.470	2.614⁽¹⁾	2.613 ⁽²⁾
	img2	2.678 ⁽²⁾	2.138	1.855	1.759	2.597	2.671	1.402	2.556	2.675 ⁽³⁾	2.583	2.683⁽¹⁾	2.607
	img3	2.553	1.983	1.820	1.402	2.528	2.612 ⁽²⁾						

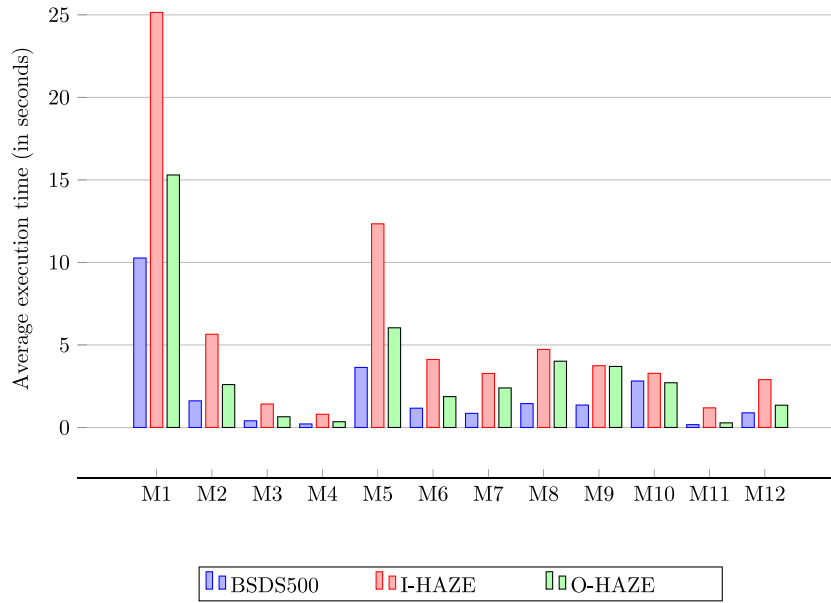


Fig. 11. Comparison of haze removal methods with respect to the execution time.

assigned to the first three methods based on their performances. The first three ranks are depicted within a bracket. All the results of Table 3 suggest that *M12* generates lower RMSE values in most of the cases as compared to *M1–M11*. However, for some images, the performance of *M6* is even better than the *M12*. However, the transmission map alone is not sufficient. The performance of all the methods would be judged based on the quality of a dehazed image.

The third experiment is conducted to compare the performances of all the methods based on the generated dehazed images. Here, the performance of each method is evaluated on three datasets namely, BSDS500, I-HAZE and O-HAZE using ten full-reference quality metrics viz., Structural Similarity Index Measure (SSIM) [60,61], Peak Signal to Noise Ratio (PSNR) [62], Mean Square Error (MSE), RMSE [59], Gradient Magnitude Similarity Deviation (GMSD) [63], BIAS, Feature SIMilarity Index (FSIM) [64], an extended form of Feature SIMilarity Index (FSIMc) [64], Riesz-transform based Feature SIMilarity (RFSIM) [65], and relative dimensionless global error (ERGAS) [66] and four no-reference quality assessment metrics namely, Blind/Referenceless image spatial quality evaluator (BRISQUE) [67], natural image quality evaluator (NIQE) [68], contrast enhancement based contrast-changed image quality measure (CEIQ) [69] and entropy (E) [70–72]. The values of SSIM, GMSD, BIAS, FSIM, FSIMc, and RFSIM vary from 0 to 1. However, the preferred value for SSIM, FSIM, FSIMc, and RFSIM is 1, likewise the preferred value of GMSD, BIAS is 0. Similarly, the value of PSNR, MSE, RMSE, ERGAS, BRISQUE, NIQE, CEIQ, and E lies in between 0 and infinity. The expected value of MSE, RMSE, ERGAS, and NIQE is 0 whereas PSNR, BRISQUE, CEIQ, and E requires a higher value. A sample image is taken from each dataset, which is displayed in Figs. 7a, 8a, and 9a, respectively. Their ground truth images are shown in Figs. 7b, 8b, and 9b. The dehazed images of Figs. 7a, 8a generated by various methods are shown in Figs. 7c–k, 8c–k, and 9c–k respectively. After analyzing the visual quality of all the dehazed images shown in Figs. 7, 8, and 9, anyone can say that the *M8* method generates much better dehazed images than others because all the images are brighter and clearer. At the same time, a drastic color-shift is also observed in the dehazed images produced by *M8*. On the other hand, a color-shift is less in the dehazed images produced by *M12*. Moreover, dehazed images achieved by the *M12* are reasonably brighter and clearer. So, we can conclude that the *M12* better restores the visual quality of a hazy image compared to *M1–M11*. However, the images that we consider

from three datasets, all are synthesized images. Therefore, methods *M1–M12* are executed on natural hazy images. Four natural haze images are downloaded from Google. Fig. 10 shows four natural images and their dehazed images obtained by *M1–M12*. It may apparently seem that the result obtained by *M3*, *M5* and *M10* are visually better, however color-shift occurred in the images and the brightness of the images have been degraded. It is clear from Fig. 10 that the *M12* better remove haze from images with a less color-shift.

As we said earlier that the quality evaluation done by HVS is not alone sufficient, so quantitative analysis is equally important. All the methods, *M1–M12*, are executed on all the images taken from BSDS500, I-HAZE, and O-HAZE datasets individually and the average values of all the fourteen metrics are reported in Tables 4, 5, and 6 respectively. Similarly, quantitative results of natural hazy images are shown in Table 7, however, ground truth images are not available for natural hazy images, therefore, no-reference metrics are only considered for evaluation. After analyzing all the results of Tables 4, 5, 6, and 7, a rank is assigned to each method, which is marked by superscript numbers. If the rank of a method is 1 it means this method is the best among all. So, Tables 4, 5, 6, and 7 illustrate that the proposed method, *M12*, comes first in most of the cases. In some cases, the *M12* is stood as either 2nd or 3rd. However, the results of other methods are not consistent, therefore, all the results demonstrate that the proposed method is relatively better than 11 state-of-the-art methods. In this study, the computation time of each method is also measured because it is also an important factor to evaluate the performance of a method. The computation time of all methods is shown in Fig. 11. The x-axis of Fig. 11 represents the name of all the methods and the proposed method and the y-axis denotes execution time in seconds. Computation time is calculated as the average of the execution time of all images of respective dataset. It can be seen that the execution time of *M12* is not pretty good, but it is acceptable.

5. Conclusion

In this study, a single image dehazing algorithm in a relatively new color channel is proposed, which consists of four steps namely, calculation of atmospheric light, transmission map, radiance, and enhancement of the dehazed image. The proposed method is capable to restore visibility of the scene. The proposed method is implemented

on six datasets namely, I-HAZE, O-HAZE, BSDS500, RESIDE, FRIDA, and Google dataset. It is compared with 11 state-of-the-art methods using fourteen quantitative evaluation metrics. The proposed method performs well on images of BSDS500 and O-HAZE datasets. On the other hand, the performance of the proposed method is satisfactory on the images taken from I-HAZE and it may happen due to block-wise atmospheric light estimation procedure. Since the block-wise atmospheric light estimation procedure selects a block from the sky region in most of the cases while computing A and there is no sky region in indoor images, therefore the value calculated as A is not precise. It may lead to performance degradation in the case of images of the I-HAZE dataset. Although the results are acceptable for indoor images, further research to generate realistic and visually pleasing images is worth conducting.

Acknowledgments

This work is partially supported by the project “Prediction of diseases through computer assisted diagnosis system using images captured by minimally-invasive and non-invasive modalities”, Computer Science and Engineering, PDPM Indian Institute of Information Technology, Design and Manufacturing, Jabalpur India (under ID: SPARC-MHRD-231). This work is also partially supported by the project at (2020/2204), Grant Agency of Excellence, University of Hradec Kralove, Faculty of Informatics and Management, Czech Republic and by the project at Universiti Teknologi Malaysia (UTM) under Research University Grant Vot-20H04, Malaysia Research University Network (MRUN) Vot 4L876 and the Fundamental Research Grant Scheme (FRGS) Vot5F073 supported under Ministry of Education Malaysia for the completion of the research.

Declaration of competing interest

The authors declare that they have no known competing financial interests or personal relationships that could have appeared to influence the work reported in this paper.

References

- [1] D. Shabna, C. Manikandababu, An efficient haze removal algorithm for surveillance video, *Int. J. Innov. Res. Sci. Eng. Technol.* 5 (5) (2016).
- [2] Gong Chen, Heqin Zhou, Jiefeng Yan, A novel method for moving object detection in foggy day, in: Eighth ACIS International Conference on Software Engineering, Artificial Intelligence, Networking, and Parallel/Distributed Computing, SNPD 2007, Vol. 2, IEEE, 2007, pp. 53–58.
- [3] Yanting Pei, Yaping Huang, Qi Zou, Yuhang Lu, Song Wang, Does haze removal help cnn-based image classification? in: Proceedings of the European Conference on Computer Vision, ECCV, 2018, pp. 682–697.
- [4] Boyi Li, Xiulian Peng, Zhangyang Wang, Jizheng Xu, Dan Feng, End-to-end united video dehazing and detection, in: Thirty-Second AAAI Conference on Artificial Intelligence, 2018.
- [5] Qi Liu, Xinbo Gao, Lihuo He, Wen Lu, Haze removal for a single visible remote sensing image, *Signal Process.* 137 (2017) 33–43.
- [6] Harald Koschmieder, Theorie der horizontalen Sichtweite, *Beitr. Phys. Freien Atmos.* (1924) 33–53.
- [7] Yoav Y. Schechner, Srinivasa G. Narasimhan, Shree K. Nayar, Instant dehazing of images using polarization, in: Proceedings of the 2001 IEEE Computer Society Conference on Computer Vision and Pattern Recognition. CVPR 2001, volume 1, IEEE, 2001, I–I.
- [8] Sarit Shwartz, Einav Namer, Yoav Y. Schechner, Blind haze separation, in: 2006 IEEE Computer Society Conference on Computer Vision and Pattern Recognition, CVPR'06, volume 2, IEEE, 2006, pp. 1984–1991.
- [9] Pu Xia, Xuebin Liu, Image dehazing technique based on polarimetric spectral analysis, *Optik* 127 (18) (2016) 7350–7358.
- [10] Guangyi Ge, Zhenzhong Wei, Jingxin Zhao, Fast single-image dehazing using linear transformation, *Optik* 126 (21) (2015) 3245–3252.
- [11] Miao Qi, Qiaohong Hao, Qingji Guan, Jun Kong, You Zhang, Image dehazing based on structure preserving, *Optik* 126 (22) (2015) 3400–3406.
- [12] Garima Yadav, Saurabh Maheshwari, Anjali Agarwal, Foggy image enhancement using contrast limited adaptive histogram equalization of digitally filtered image: Performance improvement, in: 2014 International Conference on Advances in Computing, Communications and Informatics, ICACCI, IEEE, 2014, pp. 2225–2231.
- [13] Muna F. Al-Sammaraie, Contrast enhancement of roads images with foggy scenes based on histogram equalization, in: 2015 10th International Conference on Computer Science & Education, ICCSE, IEEE, 2015, pp. 95–101.
- [14] Jiaxi He, Frank Z. Xing, Ran Yang, Cishen Zhang, Fast single image dehazing via multilevel wavelet transform based optimization, 2019, arXiv preprint [arXiv:1904.08573](https://arxiv.org/abs/1904.08573).
- [15] Asem Khmag, S.A.R. Al-Haddad, Bahareh Kalantar, et al., Single image dehazing using second-generation wavelet transforms and the mean vector L2-norm, *Vis. Comput.* 34 (5) (2018) 675–688.
- [16] Yang Wanting, Wang Ronggui, Fang Shuai, Zhang Xuan, Variable filter Retinex algorithm for foggy image enhancement, *J. Comput.-Aided Des. Comput. Graph.* 6 (010) (2010).
- [17] Wei-wei Hu, Rong-gui Wang, Shuai Fang, Qiong Hu, Retinex algorithm for image enhancement based on bilateral filtering, *J. Eng. Graph.* 2 (2010) 104–109.
- [18] T. Shu, Y.F. Liu, B. Deng, Y.P. Tan, B.Q. Chen, Multi-scale Retinex algorithm for the foggy image enhancement based on sub-band decomposition, *J. Jishou Univ.* 36 (1) (2015) 40–45.
- [19] Kaiming He, Jian Sun, Xiaoou Tang, Single image haze removal using dark channel prior, *IEEE Trans. Pattern Anal. Mach. Intell.* 33 (12) (2010) 2341–2353.
- [20] Kristofor B. Gibson, Dung T. Vo, Truong Q. Nguyen, An investigation of dehazing effects on image and video coding, *IEEE Trans. Image Process.* 21 (2) (2011) 662–673.
- [21] Shih-Chia Huang, Bo-Hao Chen, Wei-Jheng Wang, Visibility restoration of single hazy images captured in real-world weather conditions, *IEEE Trans. Circuits Syst. Video Technol.* 24 (10) (2014) 1814–1824.
- [22] Yunan Li, Qiguang Miao, Jianfeng Song, Yining Quan, Weisheng Li, Single image haze removal based on haze physical characteristics and adaptive sky region detection, *Neurocomputing* 182 (2016) 221–234.
- [23] Irfan Riaz, Teng Yu, Yawar Rehman, Hyunchul Shin, Single image dehazing via reliability guided fusion, *J. Vis. Commun. Image Represent.* 40 (2016) 85–97.
- [24] Sebastián Salazar-Colores, Juan-Manuel Ramos-Arreguín, Jesús-Carlos Pedraza-Ortega, J. Rodríguez-Reséndiz, Efficient single image dehazing by modifying the dark channel prior, *EURASIP J. Image Video Process.* 2019 (1) (2019) 66.
- [25] Ketan Tang, Jianchao Yang, Jue Wang, Investigating haze-relevant features in a learning framework for image dehazing, in: Proceedings of the IEEE Conference on Computer Vision and Pattern Recognition, 2014, pp. 2995–3000.
- [26] Qingsong Zhu, Jiaming Mai, Ling Shao, A fast single image haze removal algorithm using color attenuation prior, *IEEE Trans. Image Process.* 24 (11) (2015) 3522–3533.
- [27] Bian Gui, Yuhua Zhu, Tong Zhen, Adaptive single image dehazing method based on support vector machine, *J. Vis. Commun. Image Represent.* (2020) 102792.
- [28] Bolun Cai, Xiangmin Xu, Kui Jia, Chunmei Qing, Dacheng Tao, Dehazenet: An end-to-end system for single image haze removal, *IEEE Trans. Image Process.* 25 (11) (2016) 5187–5198.
- [29] Wenqi Ren, Si Liu, Hua Zhang, Jinshan Pan, Xiaochun Cao, Ming-Hsuan Yang, Single image dehazing via multi-scale convolutional neural networks, in: European Conference on Computer Vision, Springer, 2016, pp. 154–169.
- [30] Boyi Li, Xiulian Peng, Zhangyang Wang, Jizheng Xu, Dan Feng, Aod-net: All-in-one dehazing network, in: Proceedings of the IEEE International Conference on Computer Vision, 2017, pp. 4770–4778.
- [31] Fan Guo, Xin Zhao, Jin Tang, Hui Peng, Lijue Liu, Beiji Zou, Single image dehazing based on fusion strategy, *Neurocomputing* 378 (2020) 9–23.
- [32] Yin Gao, Yijing Su, Qiming Li, Jun Li, Single fog image restoration with multi-focus image fusion, *J. Vis. Commun. Image Represent.* 55 (2018) 586–595.
- [33] Yingying Zhu, Gaoyang Tang, Xiaoyan Zhang, Jianmin Jiang, Qi Tian, Haze removal method for natural restoration of images with sky, *Neurocomputing* 275 (2018) 499–510.
- [34] Adrian Galdran, Image dehazing by artificial multiple-exposure image fusion, *Signal Process.* 149 (2018) 135–147.
- [35] Faming Fang, Fang Li, Tieyong Zeng, Single image dehazing and denoising: A fast variational approach, *SIAM J. Imaging Sci.* 7 (2) (2014) 969–996.
- [36] Zhi Wang, Guojia Hou, Zhenkuan Pan, Guodong Wang, Single image dehazing and denoising combining dark channel prior and variational models, *IET Comput. Vis.* 12 (4) (2017) 393–402.
- [37] Guojia Hou, Jingming Li, Guodong Wang, Huan Yang, Baoxiang Huang, Zhenkuan Pan, A novel dark channel prior guided variational framework for underwater image restoration, *J. Vis. Commun. Image Represent.* 66 (2020) 102732.
- [38] Guojia Hou, Jingming Li, Guodong Wang, Zhenkuan Pan, Xin Zhao, Underwater image dehazing and denoising via curvature variation regularization, *Multimedia Tools Appl.*, 1–21.
- [39] Giuseppe Ciaburro, Neural Networks with R: smart Models using CNN, RNN, Deep Learning, and Artificial Intelligence Principles, Packt Publishing, Birmingham, UK, 2017.
- [40] Codruta O. Ancuti, Cosmin Ancuti, Radu Timofte, Christophe De Vleeschouwer, O-HAZE: A dehazing benchmark with real hazy and haze-free outdoor images, in: IEEE Conference on Computer Vision and Pattern Recognition, NTIRE Workshop, NTIRE CVPR'18, 2018.
- [41] Codruta O. Ancuti, Cosmin Ancuti, Radu Timofte, Christophe De Vleeschouwer, I-HAZE: A dehazing benchmark with real hazy and haze-free indoor images, 2018, [arXiv:1804.05091v1](https://arxiv.org/abs/1804.05091v1).

- [42] Berkeley Segmentation Data Set, Benchmarks 500 (BSDS500), 2011, URL <http://www.eecs.berkeley.edu/Research/Projects/CS/vision/grouping/resources.html>.
- [43] Boyi Li, Wenqi Ren, Dengpan Fu, Dacheng Tao, Dan Feng, Wenjun Zeng, Zhangyang Wang, Benchmarking single-image dehazing and beyond, *IEEE Trans. Image Process.* 28 (1) (2019) 492–505.
- [44] Jean-Philippe Tarel, Nicolas Hautiere, Aurélien Cord, Dominique Gruyer, Housam Halmaoui, Improved visibility of road scene images under heterogeneous fog, in: 2010 IEEE Intelligent Vehicles Symposium, IEEE, 2010, pp. 478–485.
- [45] Dong Zhao, Long Xu, Yihua Yan, Jie Chen, Ling-Yu Duan, Multi-scale optimal fusion model for single image dehazing, *Signal Process., Image Commun.* 74 (2019) 253–265.
- [46] Zhiming Tan, Xianghui Bai, Bingrong Wang, Akihiro Higashi, Fast single-image defogging, *Fujitsu Sci. Tech. J.* 50 (1) (2014) 60–65.
- [47] Yi-Jui Cheng, Bo-Hao Chen, Shih-Chia Huang, Sy-Yen Kuo, Andrey Kopylov, Oleg Seredint, Leonid Mestetskiy, Boris Vishnyakov, Yury Vizilter, Oleg Vygolov, et al., Visibility enhancement of single hazy images using hybrid dark channel prior, in: 2013 IEEE International Conference on Systems, Man, and Cybernetics, IEEE, 2013, pp. 3627–3632.
- [48] Chunxia Xiao, Jiajia Gan, Fast image dehazing using guided joint bilateral filter, *Vis. Comput.* 28 (6–8) (2012) 713–721.
- [49] Jiao Long, Zhenwei Shi, Wei Tang, Fast haze removal for a single remote sensing image using dark channel prior, in: 2012 International Conference on Computer Vision in Remote Sensing, IEEE, 2012, pp. 132–135.
- [50] Zheqi Lin, Xuansheng Wang, Dehazing for image and video using guided filter, *Appl. Sci.* 2 (2012) 123–127.
- [51] Codruta Ornatana Ancuti, Cosmin Ancuti, Single image dehazing by multi-scale fusion, *IEEE Trans. Image Process.* 22 (8) (2013) 3271–3282.
- [52] Geet Sahu, Ayan Seal, Image dehazing based on luminance stretching, in: 2019 International Conference on Information Technology, ICIT, IEEE, 2019, pp. 388–393.
- [53] Chia-Hung Yeh, Li-Wei Kang, Ming-Sui Lee, Cheng-Yang Lin, Haze effect removal from image via haze density estimation in optical model, *Opt. Express* 21 (22) (2013) 27127–27141.
- [54] Luyan Tong, Fenglin Wei, Yupeng Pan, Kai Wang, Study on the extraction of target contours of underwater images, in: International Conference on Artificial Intelligence and Security, Springer, 2020, pp. 339–349.
- [55] M. Sudhakar, M.J.anaki Meena, An efficient interactive segmentation algorithm using color correction for underwater images, *Wirel. Netw.* (2019) 1–12.
- [56] Jun Yang, Qilong Min, Weitao Lu, Ying Ma, Wen Yao, Tianshu Lu, An RGB channel operation for removal of the difference of atmospheric scattering and its application on total sky cloud detection, *Atmos. Meas. Tech.* 10 (3) (2017) 1191–1201.
- [57] Sungmin Lee, Seokmin Yun, Ju-Hun Nam, Chee Sun Won, Seung-Won Jung, A review on dark channel prior based image dehazing algorithms, *EURASIP J. Image Video Process.* 2016 (1) (2016) 4.
- [58] Jiahao Pang, Oscar C. Au, Zheng Guo, Improved single image dehazing using guided filter, in: Proc. APSIPA ASC, 2011, pp. 1–4.
- [59] Liviu Florin Zoran, Quality evaluation of multiresolution remote sensing images fusion, *UPB Sci. Bull. C* 71 (2009) 38–52.
- [60] Animesh Sengupta, Ayan Seal, Chinmaya Panigrahy, Ondrej Krejcar, Anis Yazidi, Edge information based image fusion metrics using fractional order differentiation and sigmoidal functions, *IEEE Access* 8 (2020) 88385–88398.
- [61] Chinmaya Panigrahy, Ayan Seal, Nihar Kumar Mahato, Ondrej Krejcar, Enrique Herrera-Viedma, Multi-focus image fusion using fractal dimension, *Appl. Opt.* 59 (19) (2020) 5642–5655.
- [62] Ayan Seal, Debotosh Bhattacharjee, Mita Nasipuri, Dionisio Rodríguez-Esparragón, Ernestina Menasalvas, Consuelo Gonzalo-Martín, PET-CT Image fusion using random forest and à-trous wavelet transform, *Int. J. Numer. Methods Biomed. Eng.* 34 (3) (2018) e2933.
- [63] Wufeng Xue, Lei Zhang, Xuanqin Mou, Alan C. Bovik, Gradient magnitude similarity deviation: A highly efficient perceptual image quality index, *IEEE Trans. Image Process.* 23 (2) (2013) 684–695.
- [64] Lin Zhang, Lei Zhang, Xuanqin Mou, David Zhang, FSIM: A feature similarity index for image quality assessment, *IEEE Trans. Image Process.* 20 (8) (2011) 2378–2386.
- [65] Lin Zhang, Lei Zhang, Xuanqin Mou, RFSIM: A feature based image quality assessment metric using Riesz transforms, in: 2010 IEEE International Conference on Image Processing, IEEE, 2010, pp. 321–324.
- [66] Qian Du, Nicholas H. Younan, Roger King, Vijay P. Shah, On the performance evaluation of pan-sharpening techniques, *IEEE Geosci. Remote Sens. Lett.* 4 (4) (2007) 518–522.
- [67] Anish Mittal, Anush Krishna Moorthy, Alan Conrad Bovik, No-reference image quality assessment in the spatial domain, *IEEE Trans. Image Process.* 21 (12) (2012) 4695–4708.
- [68] Anish Mittal, Rajiv Soundararajan, Alan C. Bovik, Making a “completely blind” image quality analyzer, *IEEE Signal Process. Lett.* 20 (3) (2012) 209–212.
- [69] Jia Yan, Jie Li, Xin Fu, No-reference quality assessment of contrast-distorted images using contrast enhancement, 2019, arXiv preprint [arXiv:1904.08879](https://arxiv.org/abs/1904.08879).
- [70] Chinmaya Panigrahy, Ayan Seal, Nihar Kumar Mahato, MRI and SPECT image fusion using a weighted parameter adaptive dual channel PCNN, *IEEE Signal Process. Lett.* 27 (2020) 690–694.
- [71] Chinmaya Panigrahy, Ayan Seal, Nihar Kumar Mahato, Fractal dimension based parameter adaptive dual channel PCNN for multi-focus image fusion, *Opt. Lasers Eng.* 133 (2020) 106141.
- [72] Ayan Seal, Debotosh Bhattacharjee, Mita Nasipuri, Human face recognition using random forest based fusion of à-trous wavelet transform coefficients from thermal and visible images, *AEU-Int. J. Electron. Commun.* 70 (8) (2016) 1041–1049.